# Solution Structure of Anti-HIV-1 and Anti-Tumor Protein MAP30: Structural Insights into Its Multiple Functions

Yun-Xing Wang,[1] Nouri Neamati,[2]
Jaison Jacob,[1] Ira Palmer,[3]
Stephen J. Stahl,[3] Joshua D. Kaufman,[3]
Philip Lin Huang,[4] Paul Lee Huang,[5]
Heather E. Winslow,[2] Yves Pommier,[2,8]
Paul T. Wingfield,[3] Sylvia Lee-Huang,[6,8]
Ad Bax,[7] and Dennis A. Torchia[1,8]
[1] Molecular Structural Biology Laboratory
National Institute of Dental and Craniofacial Research
National Institutes of Health
Bethesda, Maryland 20892-4310
[2] Laboratory of Molecular Pharmacology
National Cancer Institute
National Institutes of Health
Bethesda, Maryland 20892-4255
[3] Protein Expression Laboratory
National Institute of Arthritis and Musculoskeletal
    and Skin Diseases
National Institutes of Health
Bethesda, Maryland 20892
[4] American BioSciences
New York, New York 10021
[5] Department of Medicine
Massachusetts General Hospital and
Harvard Medical School
Boston, Massachusetts 02114
[6] Department of Biochemistry
School of Medicine
New York University
New York, New York 10016
[7] Laboratory of Chemical Physics
National Institute of Diabetes and Digestive
    and Kidney Diseases
National Institutes of Health
Bethesda, Maryland 20892

## Summary

We present the solution structure of MAP30, a plant protein with anti-HIV and anti-tumor activities. Structural analysis and subsequent biochemical assays lead to several novel discoveries. First, MAP30 acts like a DNA glycosylase/apurinic (ap) lyase, an additional activity distinct from its known RNA N-glycosidase activity toward the 28S rRNA. Glycosylase/ap lyase activity explains MAP30's apparent inhibition of the HIV-1 integrase, MAP30's ability to irreversibly relax supercoiled DNA, and may be an alternative cytotoxic pathway that contributes to MAP30's anti-HIV/anti-tumor activities. Second, two distinct, but contiguous, subsites are responsible for MAP30's glycosylase/ap lyase activity. Third, $Mn^{2+}$ and $Zn^{2+}$ interact with negatively charged surfaces next to the catalytic sites, facilitating DNA substrate binding instead of directly participating in catalysis.

[8] To whom correspondence should be addressed (e-mail: dtorchia@dir.nidcr.nih.gov [D. A. T.], sylvia.lee-huang@med.nyu.edu [S. L.-H.], pommier@nih.gov [Y. P.]).

## Introduction

MAP30 is a plant protein obtained from *Momordica charantia* (bitter melon), whose extracts have been used as therapeutic agents for centuries. Recent interest in MAP30 has been stimulated by reports (Lee-Huang et al., 1995a, 1995b) of (a) potent anti-tumor activity against human cancer cell lines and (b) inhibition of HIV-1 infection in lymphocytes and monocytes, and viral replication in HIV-infected cells. MAP30 toxicity is specific to tumor-transformed or viral-infected cells. It shows no adverse effects on normal cells, making it a candidate for clinical applications.

MAP30 is a ribosome-inactivating protein (RIP). RIPs inactivate ribosomes by cleaving the adenine base–ribose glycosidic bond at position A-4324 in the highly conserved $\alpha$-sarcin/ricin loop of 28S rRNA (Barbieri et al., 1993). The first RIP crystal structure solved was that of the RIP family prototype, the ricin A chain (RAC) (Montfort et al., 1987). In the putative RNA N-glycosidase (RNG) reaction mechanism, the adenine base is sandwiched by the aromatic rings of Y80 and Y123, and depurination is synchronized with protonation at the adenine $N_3$ by the Arg-180 side chain of the RAC, aided by a nearby water molecule (Monzingo and Robertus, 1992; Monzingo et al., 1993).

RIP RNG activity is distinct from anti-HIV/tumor activity (Zarling et al., 1990; Tumer et al., 1997), while MAP30 and related RIPs inhibit HIV-1 in both T cells and macrophages at concentrations that show little effect on ribosome function (Lee-Huang et al., 1990). These observations suggest that mechanisms, unrelated to ribosome inactivation, may contribute to RIP anti-HIV/tumor activities (McGrath et al., 1989; Lee-Huang et al., 1991; Nicolas et al., 1997, 1998; Tumer et al., 1997).

Various RIPs reportedly act as inefficient nucleases that cleave (a) supercoiled DNA (Li et al., 1991; Lee-Huang et al., 1995b), (b) single-stranded M13 phage DNA (Roncuzzi and GasperiCampani, 1996), and (c) supercoiled and double-stranded DNA (Huang et al., 1992; Ling et al., 1994). RIPs have also been observed to depurinate adenine in substrates, varying from double-stranded DNA and rRNA to poly(A) with a wide range of activity and specificity (Barbieri et al., 1997). This contrasts with their RNG activity, in which a specific adenine base of 28S rRNA is removed. More recently, gelonin and pokeweed antiviral protein (PAP) have been found to degrade single-stranded (ss) DNA, in the presence of $Zn^{2+}$, by first removing a protein-specific set of adenine bases from ssDNA (Nicolas et al., 1998). This step is followed by formation of the enzyme-DNA imino intermediate, characteristic of DNA glycosylase/ap lyases (DGAL), and strand cleavage at the 3′-side of the abasic sites via a $\beta$ elimination reaction (Sun et al., 1995).

As noted above, MAP30 is not cytotoxic to healthy cells. The mechanisms used by MAP30 to recognize viral-infected or tumor-transformed cells are yet to be defined. Abrin A chain and $\alpha$-sarcin are able to enter picornavirus-infected cells, once membrane properties have been altered by viral infection. In a similar fashion,

sendai virus infection renders host cells susceptible to entry by the diphtheria toxin A chain. These findings suggest that alteration of cell surface properties by viral infection is a possible mechanism for cytopathology by viruses, and MAP30 may recognize features on membranes unique to abnormal cells.

Herein, we present the high-resolution structure of MAP30. At 30 kDa, MAP30 is among the largest single-chain proteins whose solution structures have been solved without a prior X-ray crystal structure. Structural analyses combined with biochemical assays are used to derive novel insights into the multiple activities of MAP30 and other RIPs.

## Results and Discussion

### Structure Determination

On the basis of nearly complete $^1$H/$^{13}$C/$^{15}$N signal assignments, obtained using through-bond correlations (Wang et al., 1999a), we used a structure-based approach to assign over 3000 NOEs. 3D $^{15}$N and $^{13}$C separated NOESY spectra were used to identify unambiguous sequential NOEs in regular secondary structure in conjunction with the chemical shift index (Wishart and Sykes, 1994), NH $^1$H/$^2$H exchange data, and $^3$J$_{HNHA}$ couplings (Wüthrich, 1986; Vuister and Bax, 1994). 4D HNNH (Grzesiek et al., 1995a), 4D HCCH (Vuister et al., 1993), and 4D HNCH NOESY (Kay et al., 1989) spectra provided ∼1000 unambiguous medium- and long-range NOEs. The structures with the least violations calculated using these restraints were used as models to assign additional NOEs, which were then merged into the distance restraint table to calculate second generation structures. The new structures with the least restraint violations were in turn used for a new round of NOE assignments. In calculating the final set of structures, 3041 structurally significant NOEs (only 27 intraresidue) and 292 dihedral angle restraints were employed (Table 1).

Residual dipolar couplings measured in dilute liquid crystalline media (Tjandra and Bax, 1997) provide important global restraints that complement the short-range NOE and torsion angle restraints normally used in NMR structure calculations. We included 325 dipolar restraints in the structure calculation (Table 1).

Excluding 24 C terminus residues, there are ∼15 restraints per residue. These yielded an ensemble of 35 structures with no NOE or dihedral angle violations >0.3 Å or 5°, respectively. Excluding residues 240–263, the structures align well (Figure 1) with backbone and nonhydrogen atom rmsds of 0.45 ± 0.06 Å and 0.86 ± 0.05 Å, respectively, relative to the average structure, and they have good covalent geometry and small energy terms as defined by X-PLOR (Table 1). PROCHECK (Laskowski et al., 1993) revealed 85.2%, 12.3%, and 2.5% of MAP30 residues in the most favored, additionally allowed, and generously allowed regions of the ($\phi$,$\psi$) map, respectively.

### Structure of MAP30 Is Similar to that of Other RIPs

The ribbon diagram of the average solution structure (Figure 2) reveals that MAP30 adopts the RAC fold, with secondary structure similar to the crystal structures of the RAC and other RIPs (Monzingo and Robertus, 1992;

Mlsna et al., 1993; Husain et al., 1994; Xiong et al., 1997). This result is reasonable, since RIPs have homologous sequences. The N-terminal domain (residues 1–105) contains an extended mixed sheet of six β strands. Strand β3 contains the N-linked glycosylation site, N51-L52-T53, found in naturally occurring MAP30 (Lee-Huang et al., 1995b). One face of this sheet packs against α helices in the highly helical central domain (residues 108–180) of the molecule. The C-terminal domain (residues 181–263) contains a structured region in which the long bent helix, residues 181–200, packs against an antiparallel two-stranded β sheet. The ∼120° bend at N188 in the helix is supported by a ∼9.0 Hz $^3$J$_{HNHA}$ coupling constant, which is inconsistent with an α-helical $\phi$ angle.

The similarity of the solution structure of MAP30 with the crystal structures of other RIPs is borne out by the pairwise backbone coordinate rmsd values of MAP30 compared with the type II RIP RAC (3 Å) and a type I
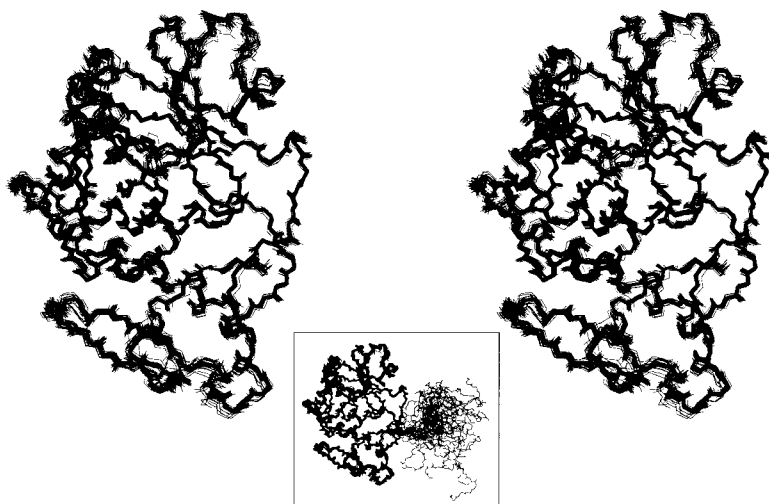
---

**Table 1. Restraints and Structural Statistics of MAP30**

**Restraints**

| | | |
|---|---|---|
| Total experimental restraints | 3926 | |
| Total distance restraints | 3299 | |
| Intraresidue (i = j) | 27 | |
| Sequential (\|i − j\| = 1) | 1094 | |
| Short range (1 < \|i − j\| ≤ 4) | 808 | |
| Long range (\|i − j\| > 4) | 1112 | |
| H bond | 258 | |
| Total dihedral restraints | 292 | |
| $\phi$ | 162 | |
| $\psi$ | 10 | |
| $\chi^1$ | 120 | |
| Total dipolar coupling constraints | 325 | |
| HNN | 165 | |
| HNC′ | 80 | |
| NC′ | 80 | |
| NOE violations >0.3 Å | 0 | |
| Dihedral angle violations >5° | 0 | |
| Accepted refined structures out of 40 | 35 | |

**Rmsds**

| Deviation from idealized geometry | {SA} | <SA>$_r$ |
|---|---|---|
| Bonds (Å) | 0.0023 ± 0.0001 | 0.0036 |
| Angles (deg.) | 0.52 ± 0.02 | 0.51 |
| Impropers (deg.) | 0.56 ± 0.1 | 0.49 |
| Backbone (1–240) rmsd (Å) | 0.45 ± 0.05 | |
| Nonhydrogen atoms (1–240) (Å) | 0.86 ± 0.05 | |
| Rmsd from residual dipolar coupling (Hz) | | |
| $^1$D$_{NH}$ | 0.79 ± 0.06 | 0.80 |
| $^1$D$_{HNC'}$ | 0.74 ± 0.08 | 0.76 |
| $^1$D$_{NC'}$ | 0.50 ± 0.06 | 0.53 |

**Energies**

| | |
|---|---|
| E(NOE) (kcal/mol) | 80.91 ± 7.0 |
| E(dihed.) (kcal/mol) | 2.28 ± 0.48 |
| E(repel) (kcal/mol) | 92.64 ± 17.03 |

Note that {SA} is the ensemble of 35 final structures; <SA>$_r$ is restrained minimized average of {SA}. With the exception of the dipolar restraints, the final values for the force constants applied for the various terms in the potential function used for the simulated annealing are the same as Garrett et al. (1997). We used an NH dipolar force constant of 0.5 kcal/mol/Hz for $^1$D$_{NH}$ and scaled the force constants for $^1$D$_{NC}$ and $^1$D$_{HNC}$ according to Ottiger and Bax (1999).

MAP30 3D NMR Solution Structure
435

Figure 1. Stereo View of the Ensemble of 35 MAP30 Structures with No NOE or Dihedral Angle Violations >0.3 Å or 5°

The backbone coordinates of residues 1–239 are superimposed. The ensemble within the box displays all 263 residues and illustrates the disordered C terminus.

RIP trichosanthin (1.7 Å) (see Additional Information). The larger rmsd for the RAC is expected because, in an approximately 240-residue alignment, MAP30 shares ~35% and ~60% sequence identity with the RAC and with trichosanthin, respectively. Regions where MAP30 and the RAC 3D structures exhibit the largest local rmsds are mostly in loops, with the least sequence homology.

The ordered structure of MAP30 terminates with residue 239; few medium-range and virtually no long-range NOEs are observed for residues 240–263. The signals of residues 240–245 are weak or absent, presumably due to exchange broadening. In addition, residues 245–263 have $^{15}$N NOEs in the range of 0.5 to −1.5, while their $^{15}$N $T_2$s are typically over twice those measured elsewhere. The C terminus had not been hydrolyzed, because its signals were not attenuated after passage of the NMR solution through a 30 kDa cutoff centrifugal filter. These results show that the 19 C-terminal residues are highly flexible on the subnanosecond time scale (Kay et al., 1989).

The flexibility of the C terminus in solution is consistent with reports that ~20 C-terminal residues are disordered in the crystal structures of type I RIPs (Irvin and Uckun, 1992; Mlsna et al., 1993; Monzingo et al., 1993; Husain et al., 1994). Nevertheless, several lines of evidence indicate that the C terminus of type I RIPs has important functions. The C terminus of PAP is reported to play a role in recognizing the cell wall (Monzingo et al., 1993) and to be required for toxicity and depurination of the tobacco ribosome in vivo, but not for antiviral activity (Tumer et al., 1998).

Although the C terminus of MAP30 is flexible, many residues of MAP30 and MAP30-C19 (MAP30 minus the C-terminal 19 residues) have different chemical shifts. Nearly all residues having different chemical shifts are on the same side of the protein as the C terminus. Despite this observation, the NOE patterns observed for MAP30 and MAP30-C19 are very similar. Taken together, these results indicate that (a) the well-structured parts of MAP30 and MAP30-C19 (residues 1–239) are similar, and (b) the flexible C terminus associates, at least transiently, with residues in the structured part of MAP30.

**Structural Features of the MAP30 RNG Active Site**
The RNG active site of the RAC (Monzingo and Robertus, 1992) and other RIPs has been identified (Monzingo et al., 1993). The sequence and structural homology of MAP30 with other RIPs reveals that residues Y70, Y109, E158, and R161 are responsible for the RNG activity of MAP30. These residues are located in a deep pocket that specifically accommodates an extrahelical adenine base. This structural feature is similar to that reported
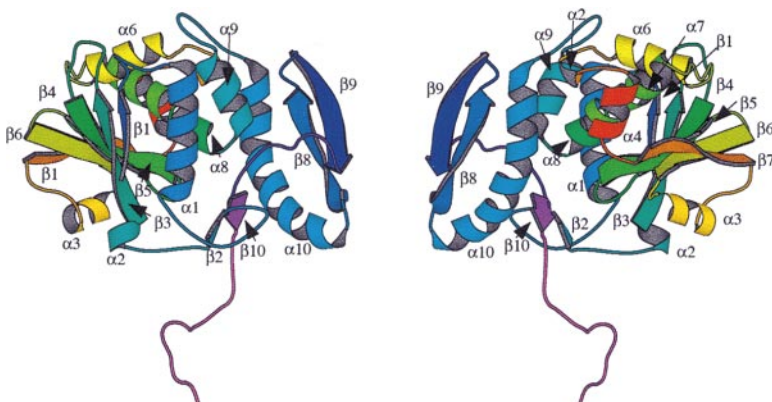


Figure 2. Ribbon Diagrams of the Minimized Average Structure of MAP30 with Secondary Structure Identified by the Program PRO-CHECK

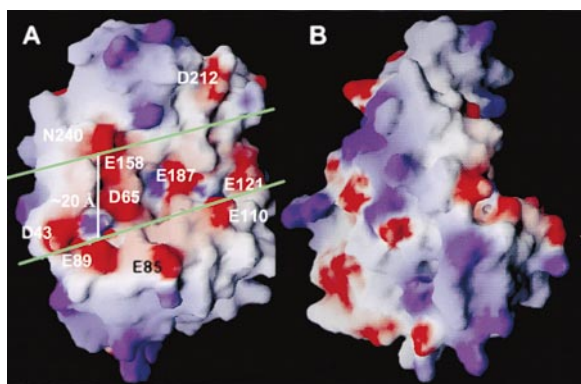The left and right views are rotated 180° relative to one another.

Figure 3. Two Views of the MAP30 Electrostatic Surface Drawn by GRASP

(A) The green lines delineate the negatively charged deep groove (ca. 20 Å wide) that crosses the surface through the deep pocket containing the RNG active site common to all RIPs.

(B) Side view of the groove obtained by an ∼90° clockwise rotation about the vertical. Molecular modeling indicates that B form DNA fits into the groove. Purple (red) surfaces have electrostatic potential greater (less) than +5 kT (−5 kT), where k is Boltzmann's constant and T the absolute temperature.

for DNA glycosylases (Savva et al., 1995; Slupphaug et al., 1996) and DGALs (Thayer et al., 1995; Vassylyev et al., 1995). The side chain of the strictly conserved R120 is close to these residues, and the arrangement of R120-E158-R161 is similar to that of the active site triad, R22-E23-R26, in T4 endonuclease V, a DGAL (Vassylyev et al., 1995). Furthermore, the MAP30 RNG pocket lies in the middle of a groove that runs along one side of the protein (Figures 3A and 3B). The surface of the groove is negatively charged with residues D43, D65, E85, and E89 to the left, and residues E110, E121, and E187 to the right of the RNG pocket. Similar grooves are found in other RIPs and are generally deeper in type I than in type II RIPs. The distance across the groove is ∼20 Å (Figures 3A and 3B), and modeling showed that a molecule of B form DNA fits into the groove. Based on these observations and the reports that RIPs have DNA activity, we hypothesized that the groove in MAP30 is a binding site for DNA substrates. To test this hypothesis, we used the HIV-1 long-terminal repeat (LTR) DNA to probe for a DNA-binding site. The LTR DNA was chosen, because Lee-Huang et al. (1995a) reported that MAP30 inhibits the action of the viral integrase against the LTR. Hence, MAP30 may bind to the LTR in competition with the viral integrase.

## Specific Residues in the MAP30 Groove Interact with the HIV LTR DNA

In order to determine whether specific residues in MAP30 interact with the HIV LTR DNA, we recorded MAP30 amide $^{15}$N and $^{1}$H chemical shifts as a function of the concentration of the LTR DNA. We overcame a precipitation problem by decreasing the MAP30 concentration to 0.1 mM and increasing the salt concentration to 175 mM, and we observed significant chemical shift perturbations for about 15 residues (Figure 4A). We note that these residues are either required for RNG activity (Y70, Y109, and E158) or surround this site (D65,
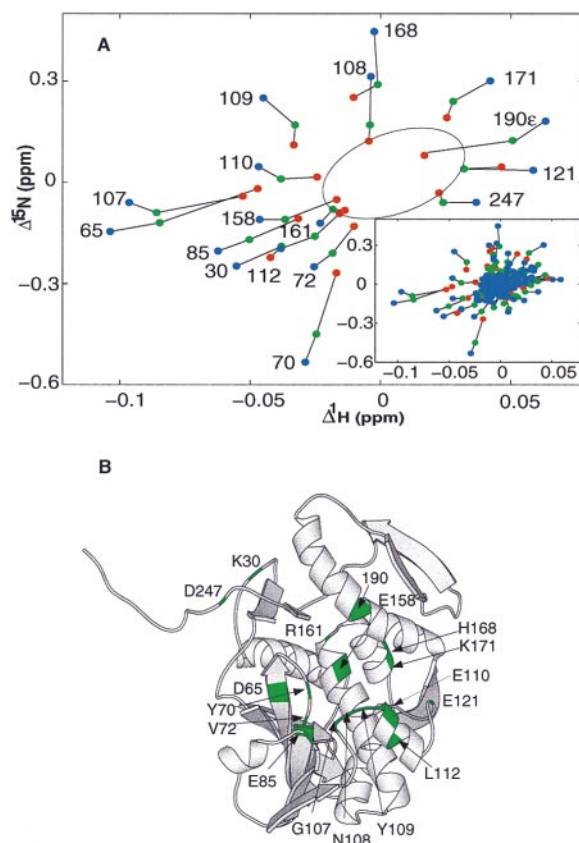

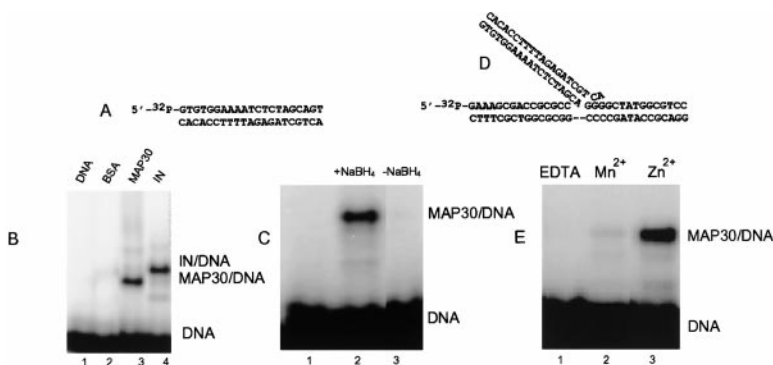


Figure 4. MAP30 Chemical Shift Perturbation by LTR DNA

(A) Changes in $^{15}$N (y axis) and $^{1}$H (x axis) amide chemical shifts of a 100 μM MAP30 solution, depicted by colored disks at DNA concentrations of 50 μM (red), 100 μM (green), and 150 μM (blue). Note that the side chain of Trp-190 was perturbed and that the vast majority of amides remaining within the oval were not strongly perturbed. (All data are shown in the lower right inset.)

(B) Ribbon diagram of MAP30 colored green to indicate residues whose chemical shifts were most sensitive (chemical shift perturbations are greater than ∼37 and ∼25 Hz in $^{1}$H and $^{15}$N dimensions, respectively) to the addition of the LTR DNA.

V71, V72, E85, G107, E110, L112, E121, K171, W190 side chain; Figures 4A and 4B). The exposed side chain of universally conserved W190 is adjacent to the RNG active site. Note that the amide signal of R161, a residue essential for RNG activity, was less perturbed than Y70, Y109, and E158 because the R161 side chain rather than backbone amide is exposed at the RNG active site.

## MAP30 Forms a Covalent Complex with the LTR DNA

The interaction of MAP30 with the LTR DNA was further probed by determining whether the protein could form a covalent enzyme–DNA intermediate similar to that formed by the HIV-1 integrase and the LTR (Mazumder et al., 1996; Neamati et al., 1998) (Figure 5). A modified $^{32}$P 5′-end-labeled 21-mer LTR DNA (Figure 5A) was made by replacing the adenine in the conserved CAGT-3′ site by uracil. This uracil-containing LTR was then treated with uracil-DNA glycosylase, yielding an intermediate containing an abasic site. This abasic site is

MAP30 3D NMR Solution Structure
437



Figure 5. Biochemical Assays of DNA Oligomers

(A) The 21-mer LTR oligonucleotide used to investigate the HIV-1 integrase/LTR DNA interaction (Neamati et al., 1998) was modified by replacing the adenine in the conserved CAGT-3′ with a uracil and was $^{32}P$ 5′-end labeled. Subsequent treatment with uracil-DNA glycosylase generated an abasic intermediate, in equilibrium with its open form isomer (Behmoaras et al., 1981). A nucleophilic attack on the aldehydic sugar residue by a lysine side chain (see end of Discussion) of MAP30 yielded a cross-linked imine intermediate, which was stabilized by reduction with sodium borohydride to give a covalently linked MAP30/LTR DNA complex.

(B) PhosphorImager picture showing formation of MAP30/LTR DNA cross-linked product. Lane 1, DNA alone; lane 2, BSA control; lane 3, MAP30/LTR DNA complex; lane 4, HIV-1 integrase/LTR DNA complex.
(C) DGAL assay showing the formation of covalent complex between MAP30 and unmodified LTR DNA. Lane 1, DNA alone; lane 2, MAP30/LTR DNA in presence of 5 mM $Zn^{2+}$ with $NaBH_4$ trapping; lane 3, MAP30+LTR DNA in presence of $Zn^{2+}$ without NaBH4 trapping.
(D) Y-shape DNA oligomer, the analog of the intermediate product of the integration reaction of the HIV-1 integrase.
(E) DGAL assay showing the formation of a covalent complex between MAP30 and unmodified Y-shape oligomer in presence of 5 mM $Mn^{2+}$ (lane 2) or 5 mM $Zn^{2+}$ (lane 3). The reactions are more efficient in presence of $Zn^{2+}$ than $Mn^{2+}$. No product was detected in the presence of EDTA (lane 1). In every gel electrophoreses, a 12% SDS–polyacrylamide gel was used. DNAs were $^{32}P$ 5′-end labeled, and the free DNAs ran at the bottom of the gel.

susceptible to nucleophilic attack on the aldehydic sugar residue by a lysine side chain (Sun et al., 1995) close to MAP30's DNA-binding site as discussed below. As seen in Figure 5B, the modified LTR DNA and MAP30 formed imino intermediates that were trapped by reduction with $NaBH_4$ for MAP30 and the HIV-1 integrase (Figure 5B, lanes 3 and 4) but not for the control, bovine serum albumin (BSA) (Figure 5B, lane 2). The UV-cross-link method also produced a MAP30/modified LTR DNA covalent complex (data not shown).

Taken together, the cross-linking and titration experiments provide complementary evidence that residues in the MAP30 groove interact with the HIV LTR DNA. Proteins that function as DNA enzymes are thought to typically use channels or grooves to interact with DNA (Jones et al., 1999).

### DNA Glycosylase/Ap Lyase Actitivity of MAP30
In addition to the report that MAP30 inhibits HIV integrase, it has been reported that RIPs cleave supercoiled DNA (Li et al., 1991; Huang et al., 1992; Ling et al., 1994; Lee-Huang et al., 1995b; Roncuzzi and GasperiCampani, 1996), and that MAP30 and gelonin (GAP31) relax supercoiled DNA irreversibly (Lee-Huang et al., 1995a, 1995b). One possible explanation for these observations is that MAP30 removes an adenine base from DNA, making it an unsuitable substrate for either HIV integrase or DNA gyrase. The removal of adenine from DNA (Barbieri et al., 1996, 1997) and our observation that LTR DNA (Figure 5A) interacts with the MAP30's depurination site led us to hypothesize that MAP30 is a DGAL. There is evidence that gelonin and PAP (Nicolas et al., 1998) are DGALs. Figure 5C (lanes 2 and 3) shows the results of a $NaBH_4$ trapping assay in which MAP30 reacts with the unmodified LTR DNA, while Figure 5E (lanes 2 and 3) shows results obtained using a Y-shaped DNA substrate (Figure 5D). In both cases a DNA-MAP30 imino intermediate is trapped by $NaBH_4$ reduction. This is evidence that MAP30 acts as a DGAL by first removing an adenine

base from each DNA substrate and then forming a covalently linked DNA/MAP30 intermediate trapped by the reduction of $NaBH_4$ (Sun et al., 1995; Nicolas et al., 1998). A detailed report of this novel MAP30 activity will be presented elsewhere.

MAP30 DGAL activity renders the HIV LTR an unsuitable substrate for the HIV integrase as well as DNA gyrase, and it may account for the apparent inhibition by MAP30 of each of the three DNA activities of the HIV-1 integrase (Lee-Huang et al., 1995b; Mazumder and Pommier, 1995). In addition, the newly discovered DGAL activity of other RIPs (Nicolas et al., 1998) and MAP30 supports proposals that RIPs have cytotoxic pathways independent of ribosome inactivation (McGrath et al., 1989; Zarling et al., 1990; Tumer et al., 1997). DGAL activity may contribute to anti-HIV/tumor activities of RIPs and may lead to a redefinition of some RIPs as DGALs (Nicolas et al., 1998) as well as ribosome inactivators.

### Function of Divalent Metal Ions
Divalent metal ions ($Ca^{2+}$, $Mg^{2+}$, $Mn^{2+}$, $Zn^{2+}$) modulate diverse activities reported for MAP30 and other RIPs. Either $Mg^{2+}$ or $Mn^{2+}$ is present in assays for reported MAP30 activities, such as inhibiting HIV-1 integrase and relaxing supercoiled DNA (Lee-Huang et al., 1995a, 1995b). DGAL activity of gelonin and PAP is mediated by $Zn^{2+}$ (Nicolas et al., 1997, 1998), while trichosanthin's DNase activity appears to be modulated by a strongly bound $Ca^{2+}$ (Li et al., 1991). In our hands, either $Mn^{2+}$ or $Zn^{2+}$ was required to detect a covalently linked Schiff base intermediate between MAP30 and DNA (Figures 5C and 5E).

It may seem puzzling that MAP30 requires a metal ion to act as either an RNG or a DGAL, since metal ions do not directly participate in either catalytic mechanism (Monzingo and Robertus, 1992; Sun et al., 1995). However, a metal ion may facilitate an enzymatic reaction by enhancing substrate binding rather than catalysis.
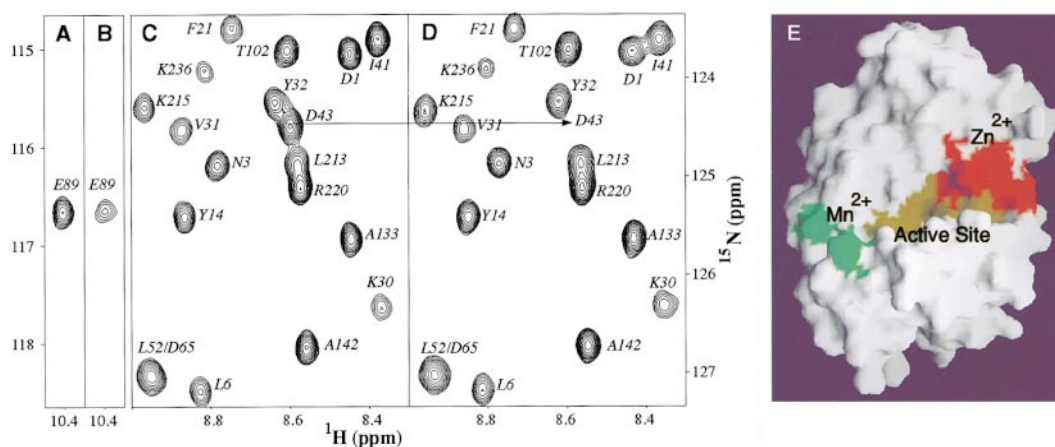
Figure 6. Metal Ion Interaction with MAP30

(A–D) Comparison of portions of MAP30 $^{15}$N-HSQC spectra recorded in the absence and presence of 600 $\mu$M Mn$^{2+}$. (A and C) No Mn$^{2+}$. (B and D) 600 $\mu$M Mn$^{2+}$. The amide signal of E89 was attenuated 8.6-fold and that of D43 disappeared at 600 $\mu$M Mn$^{2+}$. The signal of E89 disappeared at 800 $\mu$M Mn$^{2+}$.

(E) The RNG active site and the principal Mn$^{2+}$ and Zn$^{2+}$ interaction sites on the surface of MAP30. Olive green, residues Y70, Y109, E158, and R161, essential for RNG and DGAL activities. Green, residues D43 and E89 primary Mn$^{2+}$ interaction sites. Red, residues closest to the DNA-binding site (E121, I184, S185, Glu-187, and Q188) whose amide chemical-shift signals are perturbed by Zn$^{2+}$.

The electrostatic potential of MAP30 reveals negatively charged surfaces on both the left and right sides of the RNG active site (Figure 3A and Additional Information). This suggests that positively charged divalent metal ions facilitate binding of the negatively charged nucleic acids to MAP30. To check this hypothesis, we performed experiments to determine whether Mn$^{2+}$ or Zn$^{2+}$ interacts with specific regions of the MAP30 surface.

Because Mn$^{2+}$ is a paramagnetic ion, one can locate a potential Mn$^{2+}$ interaction site by monitoring the change in signal intensity (or line width) of nuclei near the bound Mn$^{2+}$. We titrated a solution of MAP30 ($\sim$0.55 mM) with MnCl$_2$ ranging in concentration from 0 to 800 $\mu$M. The titration was monitored by recording an $^1$H/$^{15}$N HSQC spectrum of MAP30 at each MnCl$_2$ concentration. The amide signal of D43 disappeared when Mn$^{2+}$ concentration reached $\sim$600 $\mu$M, while the amide signal of E89 was reduced by $\sim$10-fold at $\sim$600 $\mu$M Mn$^{2+}$ and disappeared at $\sim$800 $\mu$M Mn$^{2+}$ (Figures 6A–6E). The disappearance of these amide signals is ascribed to paramagnetic enhancement of NH transverse relaxation rates, as a consequence of the association of Mn$^{2+}$ with the carboxyl groups of D43 and E89 (Figure 3A).

Surprisingly, titration of the MAP30 solution with Zn$^{2+}$ does not perturb the chemical shifts of D43 and E89, but instead affects chemical shifts of residues in the $\alpha$9-loop-$\alpha$10 region of MAP30, on the right side of the RNG active site (Figures 3A and 6E). It has been suggested that RIP activities that require divalent metals are in fact due to contaminating nucleases (Day et al., 1998). However, the results presented herein indicate that Mn$^{2+}$ and Zn$^{2+}$ preferentially interact with certain negatively charged regions near the RNG active site of MAP30, and that they are likely to facilitate DNA binding by shielding the negative charges on the DNA backbone from the negatively charged protein surface.

## Active Sites for Depurination
## and Ap Lyase Activities
The solution structure and NMR titration data support the idea that DNA depurination and ap lyase activities

are carried out at distinct, but contiguous, subsites. We propose that one subsite is responsible for both DNA depurination and RNG activities for two reasons. First, the LTR DNA contact surface on MAP30, identified by the chemical shift titration experiment, is centered at the RNG site. The amide shifts of all four residues responsible for the RNG reaction (Y70, Y109, E158, and R161) titrate as a function of the LTR DNA concentration. Second, the MAP30 structure indicates that the adenine-binding pocket of the RNG site has a well-defined shape in solution which is well suited to accept an adenine base. This structural feature and the evidence that MAP30 and other RIPs specifically remove adenine indicate that a single adenine pocket is utilized to bind the adenine base of the tetraloop rRNA and DNA substrates. Known DNA-glycosylases or DNA-glycosylase/ap lyases recognize accessible, extrahelical bases that are either abnormal or at mismatch positions. The adenine base in the RNA tetraloop is also stacked out and accessible (Szewczak et al., 1993).

The structures of MAP30 and other RIPs suggest that the depurination active site is unsuitable as an ap lyase site because there is not a nearby amino group to serve as a nucleophile. However, an ap DNA site is expected to have greatly enhanced specific binding affinity toward aromatic side chains, based upon studies of the binding of Lys-Trp-Lys and related peptides to DNA at ap sites (Behmoaras et al., 1981). Furthermore, in every known RIP structure, the side chain of a strictly conserved Trp residue (W190 in MAP30) is found on the protein surface adjacent to the RNG site (Figure 7). We therefore propose that, following depurination, the ap DNA site binds to the side chain of the conserved Trp residue. This brings the ap site close to a lysine side chain in MAP30 (K195, Figure 7) and in PAP (K232) and gelonin (K200), two RIPs reported to have DGAL activity (Nicolas et al., 1998). This enables the lysine side chain amino group to function as an attacking nucleophile on the C1' of the ap ribose, in a manner similar to the amino groups identified as nucleophiles in DNA DGAL repair enzymes
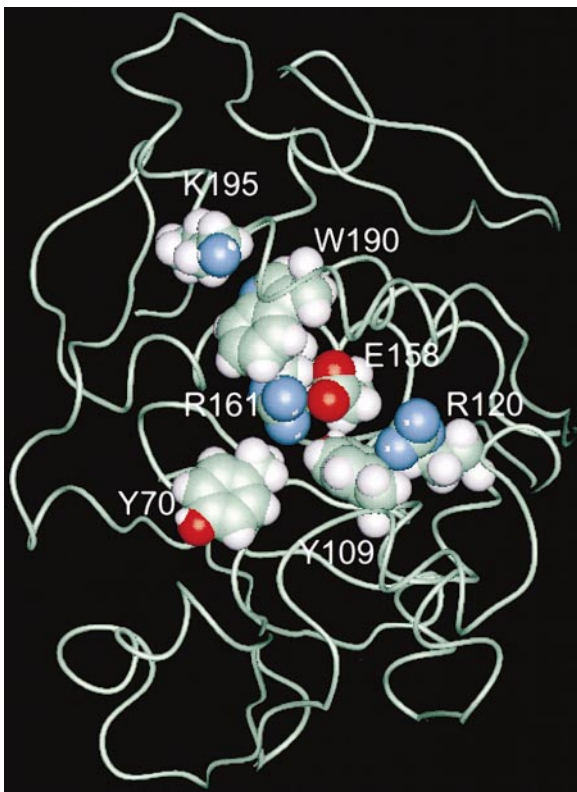
MAP30 3D NMR Solution Structure
439

and used to transfect *E. coli* DH5 cells (GIBCO–BRL). Kanamycin resistant colonies were screened for the desired deletion, and the appropriate region of candidate plasmids was sequenced (Applied Biosystems 373A DNA Sequencer). Plasmid pET-MAP30del has the sequence AAGGAGATATACATG from the ribosome-binding site to the initiation codon and was used to direct the bacterial expression of MAP30 with the natural amino terminus.

Growth of cells in minimal media supplemented with combinations of $^{15}NH_4Cl$, $^{13}C$-glucose, and $D_2O$ was performed essentially as described previously (Yamazaki et al., 1996). Cells (32 g) were resuspended using a homogenizer into 200 ml of 100 mM Tris-HCl, 1 mM EDTA, 5 mM DTT, and 1 mg/ml 4-(2-aminoethyl)-benzenesulfonyl fluoride hydrochloride (AEBSF) (pH 8.0) lysed by two passes through a French pressure cell (SLM-Aminco) at 16,000 psi then sonicated for 2 min at full power while stirring in an ice bath. The lysate was centrifuged in a Beckman JA-14 rotor at 25,000 × g for 1 hr, and the supernatant was saved and recentrifuged in a Beckman Ti-45 rotor at 125,000 × g for 1 hr. The final supernatant was applied to a 5 cm diameter × 20 cm column of DEAE Sepharose Fast Flow (Pharmacia-Biotech) equilibrated in 50 mM Tris-HCl (pH 8.0). A linear gradient (1.5 l) of 0 to 0.5 M NaCl in column buffer was applied at 5 ml/min, and 20 ml fractions were collected. Column fractions were assayed using SDS–PAGE. The majority of the MAP30 protein either did not bind or was only weakly bound to the column matrix. The column flowthrough and early eluting fractions were pooled (∼500 ml) and dialyzed against 15 l of 25 mM sodium phosphate (pH 6.5), first overnight and then with fresh buffer for a further 4–6 hr. The clear dialysate was applied to a column 5 cm diameter × 10 cm of SP Sepharose Fast Flow (Pharmacia-Biotech) equilibrated in dialysis buffer. A 2 l gradient of 0 to 1 M NaCl in column buffer was applied at 5 ml/min, and 20 ml fractions were collected. MAP30 eluted with about 0.3–0.4 M NaCl and was then concentrated to ∼20 ml using an Amicon stirred cell with a Diaflo PM10 ultrafiltration membrane (Amicon-Millipore). $\alpha_2$-macroglobulin (Boehringer Mannheim) was added (1.5–2.0 μg/mg protein) to the concentrate, which was incubated for 15–30 min prior to loading on a column 2.6 cm diameter × 100 cm of Superdex 200 (Pharmacia-Biotech) equilibrated in 50 mM Tris-HCl (pH 8.0). The column was eluted at 2 ml/min, and 6 ml fractions were collected. MAP30 was eluted in fractions between 380 ml and 410 ml and was pooled then concentrated as described above to 10 ml. Low–molecular weight contaminants were removed using a column 2.6 cm diameter × 60 cm of Superdex 75 equilibrated in 50 mM Tris-HCl (pH 8.0). Occasionally this step was repeated using Superdex 30. MAP30-C19 was purified in the same way as MAP30. Purified proteins were quantified by measuring the absorption at 280 nm in a 1 cm pathlength cell using a double-beam, diode-array Hewlett-Packard 8450A UV/VIS spectrophotometer. The optical densities at 280 nm of 1 mg/ml solutions of MAP30 and MAP30-C19 are 0.76 and 0.80, respectively



Figure 7. Backbone Trace of the MAP30 Structure with Residues in the Proposed Depurination and Ap Lyase Sites Displayed in a Space-Filling Mode

Y70, Y109, E158, R161, and probably R120 are in the subsite proposed to depurinate both RNA and DNA substrates. The spatial arrangement of R120-E158-R161 is very similar to that of the R22-E23-R26 triad found in T4 endonuclease V (Vassylyev et al., 1995). W190 and K195 are in the proposed adjacent ap lyase subsite. Following depurination, we suggest that binding of the DNA ap site to the nearby Trp side chain brings the DNA close to the amine of K195. See text for further discussion.

(Sun et al., 1995) and in peptides that cleave DNA at ap sites (Behmoaras et al., 1981). The weak ap lyase activity on single-stranded DNA reported for the RAC (Nicolas et al., 1998), which contains only two Lys residues, neither near the conserved Trp, is due to a nucleotide other than the Lys proposed herein. We note that many type I RIPs have a Lys residue, close to the conserved Trp, that can serve as a nucleophile (either at residue 192 or 195, MAP30 numbering). RNG activity and supercoiled DNA cleavage activities of PAP were simultaneously abolished by the point mutation E176V (E158V MAP30 numbering) at the depurination active site (Wang and Tumer, 1999). This observation is consistent with our model, which predicts that depurination precedes DNA chain cleavage.

## Experimental Procedures

### Preparation of Recombinant MAP30
We cloned the coding sequence of MAP30 (Lee-Huang et al., 1995a) into pET30a (+) (Novagen, Inc., Madison, WI) by cutting pMAP30 with NdeI and NcoI and treating the products with the Klenow fragment of DNA polymerase I (New England Biolabs) in the presence of dATP and dCTP. The DNA was then treated with T4 DNA ligase

### Schiff Base Cross-Link Assays
The HPLC purified oligonucleotides AE117, 5′-ACTGCTAGAGATTT TCCACAC-3′; AE118, 5′-GTGTGGAAAATCTCTAGCAGT-3′, AE157, 5′-GAAAGCGACCGCGCC-3′; AE146, 5′-GGACGCCATAGCCCCGG CGCGGTCGCTTTC-3′; AE156, 5′-GTGTGGAAAATCTCTAGCAGGG GCTATGGCGTCC-3′; and RMAB2, 5′-GTGTGGAAAATCTCTAGC UGT-3′ were purchased from Midland Certified Reagent Company (Midland, TX). To analyze the extent of cross-linking using the duplex LTR DNA, AE118 was 5′-end labeled using $T_4$ polynucleotide kinase (GIBCO–BRL) and $\gamma[^{32}P]$-ATP (Dupont-NEN). The kinase was heat inactivated, and AE117 was added to the same final concentration. To analyze the cross-linking efficiency with a Y-oligonucleotide substrate, AE157 was 5′-end labeled and annealed to AE156, AE146, and AE117. The mixture was heated at 95°C, allowed to cool slowly to room temperature, and run through a G-25 Sephadex quick spin column (Boehringer Mannheim, Indianapolis, IN) to separate annealed double-stranded oligonucleotide from unincorporated label.

To determine the Schiff base formation, RMAB2 was 5′-end labeled and reacted with AE117 as described above. The uracil was removed from duplex oligonucleotide containing deoxyuridine by incubation of 40 μl of end-labeled DNA (500 nM stock solution) with 1 U of uracil DNA glycosylase (Life Technologies, Inc.) for 90 min at 30°C. The reaction was then loaded on a G-25 Sephadex quick spin column to remove the unincorporated label and the uracil.

MAP30 (20 μM) was incubated with the appropriate oligonucleotide and divalent metal for 30 min at 30°C. A freshly prepared solution of sodium borohydride (0.1 M final concentration) was added and the reaction was continued for an additional 2 min. An equal volume (16 μl) of 2× SDS–PAGE buffer (100 mM Tris [pH 6.8], 4% 2-mercaptoethanol, 4% SDS, 0.2% bromophenol blue, 20% glycerol) was added to each reaction, and the reaction was heated at 95°C for 3 min prior to loading a 20 μl aliquot on a 12% SDS–polyacrylamide gel. The gel was run at 120 V for 1.5 hr, dried, and exposed in a PhosphorImager cassette. Gels were analyzed using a Molecular Dynamics PhosphorImager.

### Sample Conditioning and NMR Spectroscopy

The protein is a monomer with an average amide $^1H$ $T_2$ ∼17 ms at 500 MHz when dissolved in a low-salt solution at pH ∼5.5 at a concentration <0.7 mM. Above 0.7 mM, the protein tends to aggregate, as indicated by a reduction in $T_2$, and all spectra used for the structure determination were recorded at a MAP30 concentration of 0.7 mM. Assigning chemical shifts was a formidable challenge, as was expected for a 263-residue protein, containing 38 aromatic residues. Nonetheless, as reported elsewhere, we assigned over 95% of the $^1H/^{13}C/^{15}N$ chemical shifts of MAP30, including over 90% of the 38 aromatic side chain sites (Wang et al., 1999a).

Each NMR sample was dialyzed against several changes of 10 mM sodium phosphate (pH 5.5) and concentrated with a Centricon 10 (Amicon) to a volume of 260–270 μl and transferred to a Shigemi NMR tube (Shigemi, Inc.). $T_1$, $T_2$, and $^{15}N\{^1H\}$-NOEs were measured at 500 MHz in an interleaved manner (Tjandra et al., 1996) with the following: 200 complex points in f1, 512 complex points in f2, a repetition delay of 2 s (3 s for the NOE experiment), and relaxation delays $T_1$ (8, 128, 256, 448, 608, 752, 896, 1120 ms) and $T_2$ (12, 24, 36, 60, 72, 84, 96, 108 ms). The NOE was measured using the water-flip-back method and corrected for the finite repetition delay (Grzesiek and Bax, 1993). Relaxation rates were obtained by fitting the peak intensities to a two-parameter exponential function.

### Chemical Shift Perturbation Experiments

$^{15}N$-HSQC MAP30 spectra were recorded as a function of metal ion or LTR DNA concentration. In the titration with $Mn^{2+}$, MAP30 (∼0.55 mM containing ∼10 μM EDTA) was added with $MnCl_2$ (Sigma) at concentrations of 50, 100, 200, 400, 600, and 800 μM. In the titration with $Zn^{2+}$, MAP30 (∼0.7 mM containing ∼10 μM EDTA) was titrated with $ZnSO_4$ (Sigma) at concentrations of 0.1, 0.2, 0.4, 0.5, 0.8, 1.0, and 1.5 mM. At a $Zn^{2+}$ concentration greater than ∼0.5–1 mM, a precipitate, identified as zinc phosphate, formed. For this reason, the titration experiment was repeated at pH 5.5, replacing the phosphate buffer with citrate, using $Zn^{2+}$ concentrations of 0.5, 1.0, 1.5, and 3.0 mM. No precipitate was observed, and the same residues whose chemical shifts were perturbed upon addition of $Zn^{2+}$ in the phosphate buffer were perturbed in the citrate buffer. MAP30 (0.1 mM) was titrated with the LTR DNA (Integrated Technology) at concentrations of 0.05, 0.1, and 0.15 mM in the presence of 10 μM EDTA, 175 mM NaCl. The DNA used in the titration was desalted, and the pH of the solution was adjusted to 5.5 with a NaOH or HCl before each HSQC spectrum was recorded.

### Dipolar Coupling Measurements

We measured $^1D_{NH}$, $^1D_{NC'}$, and $^2D_{HC'}$ dipolar couplings for $^{15}N/^2H$ and $^{13}C/^{15}N/^2H$ MAP30 samples. Two different concentrations of liquid crystalline media were used (Wang et al., 1998), consisting of an aqueous mixture of either 5% or 6% 3:1 dimyristoyl-phosphatidylcholine (DMPC):dihexanoyl-phosphatidylcholine (DHPC). The axial (A) and rhombic (R) components of D obtained from the powder pattern of each data set (Clore et al., 1998) were A = −17.6 Hz, R = 0.58 in the 6% medium, and A = −16.1 Hz, R = 0.66 in the 5% medium. Normalization factors (Ottiger and Bax, 1999) were used to scale the different types of dipolar couplings. MAP30 structures were refined against the two independent alignment tensors.

### Hydrogen Bond Measurements

We measured $^{3h}J_{NC'}$ connectivity across hydrogen bonds using a perdeuterated $^2H/^{13}C/^{15}N$-labeled MAP30 sample, allowing us to identify unambiguously donor and acceptor atoms involved in hydrogen bonds, as described elsewhere (Wang et al., 1999b).

### Structure Calculations

We calculated the structure of MAP30 using simulated annealing in torsion angle space (Stein et al., 1997) starting from an extended strand, followed by simulated annealing in Cartesian space (Nilges et al., 1988) using a modified XPLOR 3.5, containing pseudopotentials for residual dipolar coupling (Tjandra et al., 1997) and a conformational database (Kuszewski et al., 1997). Hydrogen bond constraints, two for each hydrogen bond (NH–O = 1.5–2.8 Å and N–O = 2.4–3.5 Å), were derived from NH exchange experiments, backbone NOE patterns, backbone $C_\alpha/C_\beta$ chemical shifts, and direct measurements of $^{3h}J_{NC'}$ connectivity across hydrogen bonds and applied in the later stage of the structure calculation. $\phi$ and $\psi$ angles were derived from three-bond $^3J_{HNHA}$ coupling constants, measured with the 3D HNHA experiment (Vuister and Bax, 1994) and a database analysis of backbone ($^1H$, $^{15}N$, $^{13}C_\alpha$, $^{13}C_\beta$, and C') chemical shifts, using the program TALOS (Cornilescu et al., 1999). The $\phi$ dihedral angle was restrained to $-60° \pm 30°$ if $J_{HNHA} < 5.5$ Hz or to $110° \pm 50°$ if $J_{HNHA} > 8.0$ Hz. $\chi1$ dihedral angles and stereo-specific assignments of β-methylene protons were derived from $J_{HNHB}$ and $J_{HAHB}$ scalar coupling constants obtained from 3D HNHB and HACAHB-COSY experiments (Archer et al., 1991; Grzesiek et al., 1995b). Tight turns clearly identified by NOE patterns and J-coupling constants, $\phi$ and $\psi$ angles were restrained to their standard values with $\pm30°$ error range (Wüthrich, 1986). For residues having intense intraresidue HN-H$_\alpha$ NOEs with positive $\phi$ angles suggested by the program TALOS (Cornilescu et al., 1999), $\phi$ was restrained to $40° \pm 15°$ (Garrett et al., 1997). Electrostatic surfaces were calculated using GRASP (Nicholls et al., 1991). Molecular models were generated with Quanta (MSI), Insight (MSI), and MOLSCRIPT (Kraulis, 1991).

### Additional Information

MAP30 and MAP30-C19 chemical shifts, coordinate rmsd comparisons of MAP30 with other RIPs, RIP sequence alignments and electrostatic surface potentials, and a plot of DNA chemical shift titration versus residue number are available from the authors.

### References

Archer, S.J., Ikura, M., Torchia, D.A., and Bax, A. (1991). An alternative 3D-NNR technique for correlating backbone $^{15}N$ with side-chain H-beta-resonances in larger proteins. J. Magn. Reson. *95*, 636–641.

Barbieri, L., Battelli, M.G., and Stirpe, F. (1993). Ribosome-inactivating proteins from plants. Biochim. Biophy. Acta *1154*, 237–282.

Barbieri, L., Valbonesi, P., Gorini, P., Pession, A., and Stirpe, F. (1996). Polynucleotide:adenosine glycosidase activity of saporin-L1: effect on DNA, RNA and poly(A). Biochem. J. *319*, 507–513.

Barbieri, L., Valbonesi, P., Bonora, E., Gorini, P., Bolognesi, A., and Stirpe, F. (1997). Polynucleotide:adenosine glycosidase activity of ribosome-inactivating proteins: effect on DNA, RNA and poly(A). Nucleic Acids Res. *25*, 518–522.

Behmoaras, T., Toulme J-J., and Helene, C. (1981). A tryptophan-containing peptide recognizes and cleaves DNA at apurinic sites. Nature *292*, 858–859.

Clore, G.M., Gronenborn, A.M., and Bax, A. (1998). A robust method for determining the magnitude of the fully asymmetric alignment tensor of oriented macromolecules in the absence of structural information. J. Magn. Reson. *133*, 216–221.

MAP30 3D NMR Solution Structure
441

Cornilescu, G., Delaglio, F., and Bax, A. (1999). Protein backbone angle restraints from searching a database for chemical shift and sequence homology. J. Biomol. NMR 13, 289–302.

Day, P.J., Lord, J.M., and Roberts, L.M. (1998). The deoxyribonucle-ase activity attributed to ribosome-inactivating proteins is due to contamination. Eur. J. Biochem. 258, 540–545.

Garrett, D.S., Seok, Y.J., Liao, D.I., Peterkofsky, A., Gronenborn, A.M., and Clore, G.M. (1997). Solution structure of the 30 kDa N-ter-minal domain of enzyme I of the Escherichia coli phosphoenolpy-ruvate:sugar phosphotransferase system by multidimensional NMR. Biochemistry 36, 2517–2530.

Grzesiek, S., and Bax, A. (1993). Measurement of amide proton-exchange rates and NOEs with water in $^{13}$C/$^{15}$N-enriched calcineu-rin-B. J. Biomol. NMR 3, 627–638.

Grzesiek, S., Kuboniwa, H., Hinck, A.P., and Bax, A. (1995a). Multi-ple-quantum line narrowing for measurement of H$^\alpha$-H$^\beta$ J-couplings in isotopically enriched proteins. J. Am. Chem. Soc. 117, 5312–5315.

Grzesiek, S., Wingfield, P., Stahl, S., Kaufman, J.D., and Bax, A. (1995b). 4-Dimensional $^{15}$N-separated NOESY of slowly tumbling perdeuterated $^{15}$N-enriched proteins—application to HIV-1 Nef. J. Am. Chem. Soc. 117, 9594–9595.

Huang, P.L., Chen, H.C., Kung, H.F., Huang, P., Huang, H.I., and Lee-Huang, S. (1992). Anti-HIV plant-proteins catalyze topological changes of DNA into inactive forms. Biofactors 4, 37–41.

Husain, J., Tickle, I.J., and Wood, S.P. (1994). Crystal-structure of momordin, a type-I ribosome-inactivating protein from the seeds of momordica-charantia. FEBS Lett. 342, 154–158.

Irvin, J.D., and Uckun, F.M. (1992). Pokeweed antiviral protein-ribo-some inactivation and therapeutic applications. Pharmacol. Ther. 55, 279–302.

Jones, S., van Heyningen, P., Berman, H.M., and Thornton, J.M. (1999). Protein-DNA interactions: a structural analysis. J. Mol. Biol. 287, 877–896.

Kay, L.E., Torchia, D.A., and Bax, A. (1989). Backbone dynamics of proteins as studied by $^{15}$N inverse detected heteronuclear NMR-spectroscopy: application to staphylococcal nuclease. Biochemis-try 28, 8972–8979.

Kraulis, P.J. (1991). MOLSCRIPT: a program to produce both de-tailed and schematic plots of protein structures. J. Appl. Crystallogr. 24, 946–950.

Kuszewski, J., Gronenborn, A.M., and Clore, G.M. (1997). Improve-ments and extensions in the conformational database potential for the refinement of NMR and X-ray structures of proteins and nucleic acids. J. Magn. Reson. 125, 171–177.

Laskowski, R.A., Macarthur, M.W., Moss, D.S., and Thornton, J.M. (1993). Procheck: a program to check the stereochemical quality of protein structures. J. Appl. Crystallogr. 26, 283–291.

Lee-Huang, S., Huang, P.L., Nara, P.L., Chen, H.C., Kung, H.F., Huang, P., and Huang, H.I. (1990). MAP30: a new inhibitor of HIV-1 infection and replication. FEBS Lett. 272, 12–18.

Lee-Huang, S., Kung, H.F., Huang, P.L., Li, B.Q., Huang, P., Huang, H.I., and Chen, H.C. (1991). A new class of anti-HIV agents: GAP-31, DAP-30 and DAP-32. FEBS Lett. 291, 139–144.

Lee-Huang, S., Huang, P.L., Bourinbaiar, A.S., Chen, H.C., and Kung, H.F. (1995a). Inhibition of the integrase of human-immunodefi-ciency-virus (HIV) type-1 by anti-HIV plant-proteins MAP30 and GAP31. Proc. Natl. Acad. Sci. USA 92, 8818–8822.

Lee-Huang, S., Huang, P.L., Chen, H.C., Bourinbaiar, A., Huang, H.I., and Kung, H.F. (1995b). Anti-HIV and anti-tumor activities of recombinant MAP30 from bitter-melon. Gene 161, 151–156.

Li, M.X., Yeung, H.W., Pan, L.P., and Chan, S.I. (1991). Trichosanthin, a potent HIV-1 inhibitor, can cleave supercoiled DNA in vitro. Nucleic Acids Res. 19, 6309–6312.

Ling, J., Liu, W.Y., and Wang, T.P. (1994). Cleavage of supercoiled double-stranded DNA by several ribosome-inactivating proteins in-vitro. FEBS Lett. 345, 143–146.

Mazumder, A., and Pommier, Y. (1995). Processing of deoxyluridine mismatches and abasic sites by human immunodeficiency virus type-1 integrase. Nucleic Acids Res. 23, 3865–2871.

Mazumder, A., Neamati, N., Pilon, A.A., Sunder, S., and Pommier, Y. (1996). Chemical trapping of ternary complexes of human immu-nodeficiency virus type I integrase, divalent metal, and DNA sub-strates containing an abasic site: implications for the role of lysine 136 in DNA binding. J. Biol. Chem. 271, 27330–27338.

McGrath, M.S., Hwang, K.M., Caldwell, S.E., Gaston, I., Luk, K.C., Wu, P., Ng, V.L., Crowe, S., Daniels, J., Marsh, J., et al. (1989). GLQ223: an inhibitor of human immunodeficiency virus-replication in acutely and chronically infected-cells of lymphocyte and mononu-clear phagocyte lineage. Proc. Natl. Acad. Sci. USA 86, 2844–2848.

Mlsna, D., Monzingo, A.F., Katzin, B.J., Ernst, S., and Robertus, J.D. (1993). Structure of recombinant ricin A-chain at 2.3 angstrom. Protein Sci. 2, 429–435.

Montfort, W., Villafranca, J.E., Monzingo, A.F., Ernst, S.R., Katzin, B., Rutenber, E., Xuong, N.H., Hamlin, R., and Robertus, J.D. (1987). The 3-dimensional structure of ricin at 2.8-Å. J. Biol. Chem. 262, 5398–5403.

Monzingo, A.F., and Robertus, J.D. (1992). X-ray-analysis of sub-strate-analogs in the ricin A-chain active-site. J. Mol. Biol. 227, 1136–1145.

Monzingo, A.F., Collins, E.J., Ernst, S.R., Irvin, J.D., and Robertus, J.D. (1993). The 2.5 angstrom structure of pokeweed antiviral pro-tein. J. Mol. Biol. 233, 705–715.

Neamati, N., Hong, H., Owen, J.M., Sunder, S., Winslow, H.E., Chris-tensen, J.L., Zhao, H., Burke, T.R., Milne, G.W.A., and Pommier, Y. (1998). Salicylhydrazine-containing inhibitors of HIV-1 integrase: implication for a selective chelation in the integrase active site. J. Med. Chem. 41, 3202–3209.

Nicholls, A., Sharp, K.A., and Honig, B. (1991). Protein folding and association-insights from the interfacial and thermodynamic proper-ties of hydrocarbons. Proteins 11, 281–296.

Nicolas, E., Goodyer, L.D., and Taraschi, T.F. (1997). An additional mechanism of ribosome-inactivating protein cytotoxicity: degrada-tion of extrachromosomal DNA. Biochem. J. 327, 413–417.

Nicolas, E., Beggs, J.M., Haltiwanger, B.M., and Taraschi, T.F. (1998). A new class of DNA glycosylase apurinic/apyrimidinic lyases that act on specific adenines in single-stranded DNA. J. Biol. Chem. 273, 17216–17220.

Nilges, M., Clore, G.M., and Gronenborn, A.M. (1988). Determination of 3-dimensional structures of proteins from interproton distance data by dynamical simulated annealing from a random array of atoms: circumventing problems associated with folding. FEBS Lett. 239, 129–136.

Ottiger, M., and Bax, A. (1999). Bicelle-based liquid crystals for NMR-measurement of dipolar couplings at acidic and basic pH values. J. Biomol. NMR 13, 187–191.

Roncuzzi, L., and GasperiCampani, A. (1996). DNA-nuclease activity of the single-chain ribosome-inactivating proteins dianthin 30, sa-porin 6 and gelonin. FEBS Lett. 392, 16–20.

Savva, R., McAuleyhecht, K., Brown, T., and Pearl, L. (1995). The structural basis of specific base-excision repair by uracil-DNA gly-cosylase. Nature 373, 487–493.

Slupphaug, G., Mol, C.D., Kavli, B., Arvai, A.S., Krokan, H.E., and Tainer, J.A. (1996). A nucleotide-flipping mechanism from the struc-ture of human uracil-DNA glycosylase bound to DNA. Nature 384, 87–92.

Stein, E.G., Rice, L.M., and Brunger, A.T. (1997). Torsion-angle mo-lecular dynamics as a new efficient tool for NMR structure calcula-tion. J. Magn. Reson. 124, 154–164.

Sun, B., Latham, K.A., Dodson, M.L., and Lloyd, R.S. (1995). Studies on the catalytic mechanism of 5 DNA glycosylases: probing for enzyme-DNA imino intermediates. J. Biol. Chem. 270, 19501–19508.

Szewczak, A.A., Moore, P.B., Chang, Y.L., and Wool, I.G. (1993). The conformation of the sarcin/ricin loop from 28S ribosomal RNA. Proc. Natl. Acad. Sci. USA 90, 9581–9585.

Thayer, M.M., Ahern, H., Xing, D.X., Cunningham, R.P., and Tainer, J.A. (1995). Novel DNA-binding motifs in the DNA-repair enzyme endonuclease-III crystal-structure. EMBO J. 14, 4108–4120.

Tjandra, N., and Bax, A. (1997). Direct measurement of distances and angles in biomolecules by NMR in a dilute liquid crystalline medium. Science 278, 1111–1114.

Tjandra, N., Szabo, A., and Bax, A. (1996). Protein backbone dynamics and $^{15}$N chemical shift anisotropy from quantitative measurement of relaxation interference effects. J. Am. Chem. Soc. *118*, 6986–6991.

Tjandra, N., Garrett, D.S., Gronenborn, A.M., Bax, A., and Clore, G.M. (1997). Defining long range order in NMR structure determination from the dependence of heteronuclear relaxation times on rotational diffusion anisotropy. Nat. Struct. Biol. *4*, 443–449.

Tumer, N.E., Hwang, D.J., and Bonness, M. (1997). C-terminal deletion mutant of pokeweed antiviral protein inhibits viral infection but does not depurinate host ribosomes. Proc. Natl. Acad. Sci. USA *94*, 3866–3871.

Tumer, N.E., Parikh, B.A., Li, P., and Dinman, J.D. (1998). The pokeweed antiviral protein specifically inhibits Ty1- directed +1 ribosomal frameshifting and retrotransposition in Saccharomyces cerevisiae. J. Virol. *72*, 1036–1042.

Vassylyev, D.G., Kashiwagi, T., Mikami, Y., Ariyoshi, M., Iwai, S., Ohtsuka, E., and Morikawa, K. (1995). Atomic model of a pyrimidine dimer excision-repair enzyme complexed with a DNA substrate-structural basis for damaged DNA recognition. Cell *83*, 773–782.

Vuister, G.W., and Bax, A. (1994). Measurement of 4-bond H(N)-H-alpha J-couplings in staphylococcal nuclease. J. Biomol. NMR *4*, 193–200.

Vuister, G.W., Clore, G.M., Gronenborn, A.M., Powers, R., Garrett, D.S., Tschudin, R., and Bax, A. (1993). Increased resolution and improved spectral quality in 4- dimensional C-13/C-13-separated HMQC-NOESY-HMQC spectra using pulsed-field gradients. J. Magn. Reson. Ser. B *101*, 210–213

Wang, P., and Tumer, N.E. (1999). Pokeweed antiviral protein cleaves double-stranded supercoiled DNA using the same active site required to depurinate rRNA. Nucleic Acids Res. *27*, 1900–1905.

Wang, Y.X., Marquardt, J.L., Wingfield, P., Stahl, S.J., Lee-Huang, S., Torchia, D., and Bax, A. (1998). Simultaneous measurement of $^1$H-$^{15}$N, $^1$H, $^{13}$C′, and $^{15}$N-$^{13}$C′ dipolar couplings in a perdeuterated 30 kDa protein dissolved in a dilute liquid crystailine phase. J. Am. Chem. Soc. *120*, 7385–7386.

Wang, Y.X., Jacob, J., Wingfield, P.T., Palmer, I., Stahl, S.J., Kaufman, J.D., Huang, P.L., Huang, P.L, Lee-Huang, S., and Torchia, D.A. (1999a). Anti-HIV and anti-tumor protein MAP30, a 30 kDa single-strand type-I RIP, shares similar secondary structure and β-sheet topology with the A chain of ricin, a type-II RIP. Protein Sci., in press.

Wang, Y.X., Jacob, J., Cordier, F., Wingfield, P., Stahl, S.J., Lee-Huang, S., Torchia, D., Grzesiek, S., and Bax, A. (1999b). Measurement of ($^{3h}$)J(NC′) connectivities across hydrogen bonds in a 30 kDa protein. J. Biomol. NMR *14*, 181–184.

Wishart, D.S., and Sykes, B.D. (1994). Chemical-shifts as a tool for structure determination. In Methods in Enzymology, T.L. James and N.J. Oppenheimer, eds. (San Diego, CA: Academic Press) *239*, 363–392.

Wüthrich, K. (1986). NMR of Proteins and Nucleic Acids (New York: John Wiley).

Xiong, J.P., Xi, Z.X., and Wang, Y. (1997). Crystal structure of the complex of trichosanthin with NADPH at 0.172 nm resolution. Chin. J. Chem. *15*, 265–277.

Yamazaki, T., Hinck, A.P., Wang, Y.X., Nicholson, L.K., Torchia, D.A., Wingfield, P., Stahl, S.J., Kaufman, J.D., Chang, C.H., Domaille, P.J., and Lam, P.Y.S. (1996). Three-dimensional solution structure of the HIV-1 protease complexed with DMP323, a novel cyclic urea-type inhibitor, determined by nuclear magnetic resonance spectroscopy. Protein Sci. *5*, 495–506.

Zarling, J.M., Moran, P.A., Haffar, O., Sias, J., Richman, D.D., Spina, C.A., Myers, D.E., Kuebelbeck, V., Ledbetter, J.A., and Uckun, F.M. (1990). Inhibition of HIV replication by pokeweed antiviral protein targeted to CD4+ cells by monoclonal-antibodies. Nature *347*, 92–95.

**Protein Data Bank ID Code**

The coordinates of the MAP30 NMR structure have been deposited with the ID code 1d8v.